AGU PUBLICATIONS

JGR

Journal of Geophysical Research: Solid Earth

RESEARCH ARTICLE

10.1002/2013JB010290

Key Points:
- Sonic velocity measurements conducted during triaxial deformation tests
- Improved data processing of sonic velocity measurements
- Differentiation of variably consolidated sediments using acoustic properties

Supporting Information:
- Readme
- Text S1
- Figure S1
- Figure S2
- Figure S3

Correspondence to:
K. Schumann,
kaschumann@geomar.de

Citation:
Schumann, K., M. Stipp, J. H. Behrmann, D. Klaeschen, and D. Schulte-Kortnack (2014), *P* and *S* wave velocity measurements of water-rich sediments from the Nankai Trough, Japan, *J. Geophys. Res. Solid Earth*, *119*, 787–805, doi:10.1002/2013JB010290.

Received 16 APR 2013
Accepted 4 JAN 2014
Accepted article online 10 JAN 2014
Published online 7 FEB 2014

P and *S* wave velocity measurements of water-rich sediments from the Nankai Trough, Japan

Kai Schumann[1], Michael Stipp[1], Jan H. Behrmann[1], Dirk Klaeschen[1], and Detlef Schulte-Kortnack[2]

[1]Marine Geodynamics, GEOMAR Helmholtz Centre for Ocean Research Kiel, Kiel, Germany, [2]Institute of Geosciences, Kiel University, Kiel, Germany

Abstract Acoustic velocities were measured during triaxial deformation tests of silty clay and clayey silt core samples from the Nankai subduction zone (Integrated Ocean Drilling Program Expeditions 315, 316, and 333). We provide a new data set, continuously measured during pressure increase and subsequent axial deformation. A new data processing method was developed using seismic time series analysis. Compressional wave velocities (V_p) range between about 1450 and 2200 m/s, and shear wave velocities (V_s) range between about 150 and 800 m/s. V_p slightly increases with rising effective confining pressure and effective axial stress. Samples from the accretionary prism toe show the highest *Vp*, while fore-arc slope sediments show lower *Vp*. Samples from the incoming plate, slightly richer in clay minerals, have the lowest values for V_p. V_s increases with higher effective confining pressures and effective axial stress, irrespective of composition and tectonic setting. Shear and bulk moduli are between 0.2 and 1.3 GPa, and 3.85 and 8.41 GPa, respectively. Elastic moduli of samples from the accretionary prism toe and the footwall of the megasplay fault (1.50 and 3.98 GPa) are higher than those from the hanging wall and incoming plate (0.59 and 0.88 GPa). This allows differentiation between normal and overconsolidated sediments. The data show that in a tectonosedimentary environment of only subtle compositional differences, acoustic properties can be used to differentiate between stronger (accretionary prism toe) and weaker (fore-arc slope, incoming plate) sediments. Especially V_p/V_s ratios may be instrumental in detecting zones of low effective stress and thus high pore fluid pressure.

1. Introduction

The Nankai accretionary complex, located at the Pacific side of SW Japan (Figure 1a), belongs to one of the most intensively studied subduction zones on Earth. In this region, the Philippine Sea plate is subducted beneath the Eurasian plate with a convergence azimuth of ~80° [e.g., *Taira et al*., 1991] and a dip angle of 10° to 22° [e.g., *Xu and Kono*, 2002]. Over the historical record, earthquakes of magnitude > 8 repeatedly occurred in this region with intervals of 100 to 200 years [e.g., *Ando*, 1975; *Park et al*., 2002a]. This has led to the planning and implementation of the Nankai Trough Seismogenic Zone Experiment (NanTroSEIZE), forming part of the Integrated Ocean Drilling Program (IODP). NanTroSEIZE is designed to drill, to sample, and to monitor the plate boundary thrust and elucidate earthquake-generating processes around the updip end of the seismogenic zone. Drilling into the seismogenic portion of the plate boundary yields the possibility to sample deformed rocks from a recently seismically active fault zone, which ruptured during the 1944 Tonankai earthquake [*Tobin and Kinoshita*, 2006]. The mechanical characteristics of these rocks directly control the strength and frictional behavior of faults in accretionary prisms and thus play a key role in earthquake rupture dynamics [e.g., *Scholz*, 2002]. To determine the mechanical characteristics in laboratory tests, drilling and sampling of fault zones at depth is essential.

In the case of the Nankai trench, the initially unlithified sediments of the Philippine Sea Plate are scraped off and added to the accretionary prism at the leading edge of the overriding Eurasian plate. A slope of clastic sediments derived from the Japanese Islands lies on top of the accreted sediments. Compaction and dewatering within the accretionary prism caused by progressive burial and tectonic deformation results in changing physical properties [e.g., *Carson et al*., 1982; *Moore and Vrolijk*, 1992; *Erickson and Jarrard*, 1998; *Bilek and Lay*, 1999; *Moore and Saffer*, 2010], such as porosity, density, shear strength, and compressibility. Mechanical compaction at shallow depth and low temperatures is mainly a function of effective confining pressure, before becoming dominantly controlled by diagenetic mineralogical and fabric changes toward greater depth [e.g., *Mondol et al*., 2007]. Lithological and mechanical properties were determined in order to relate these to elastic wave velocities and their changes during experimental deformation. Seismic time series

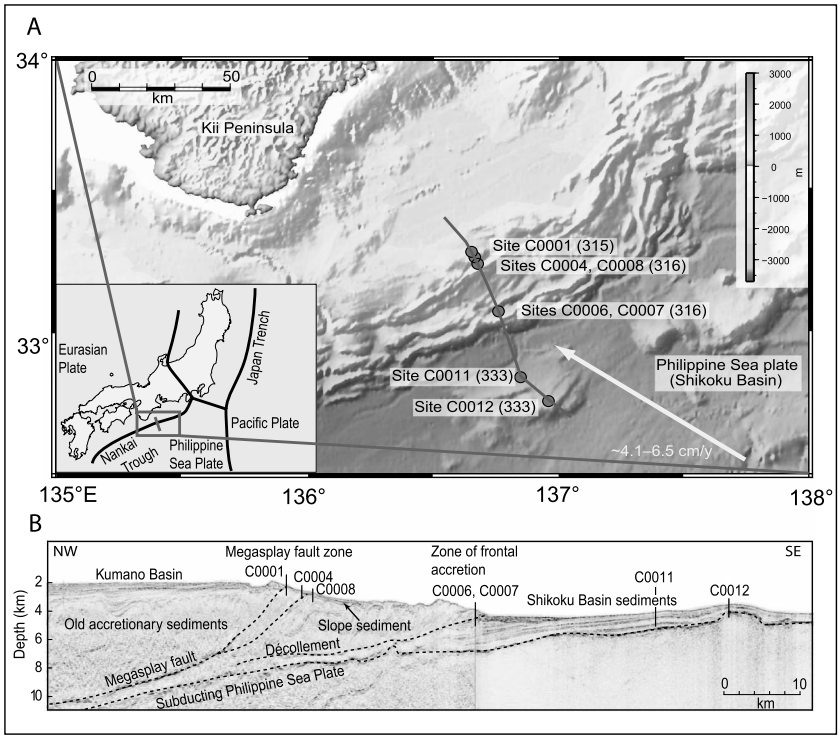

Figure 1. (a) Tectonic setting and the location of the Nankai Trough (inset) and detailed bathymetric map [*Becker et al.*, 2009] of the Kumano Basin showing the locations of the IODP drill sites (dots; expedition numbers are given in brackets) along the seismic profile. The arrow indicates the plate convergence direction. (b) Seismic profile across the Nankai accretionary complex [after *Kinoshita et al.*, 2012]. IODP drill sites are projected onto the profile. IODP Sites C0011 and C0012 are located on the incoming plate.

analysis was applied to sonic velocity measurements, enabling fast processing and good detection of first arrivals. We chose samples from different tectonosedimentary environments at the Nankai trench and forearc to investigate the question whether incoming sediment on the oceanic plate, sediment cover of the frontal thrust zone, and the megasplay setting possess distinct acoustic characteristics. Measurements during the experimental deformation stages were conducted in order to quantify the effects of fabric changes on the acoustic properties that would be associated with tectonic shearing of the sediments.

2. Geological Setting and Sample Description

The growth of the Japanese Island arc system was initiated in the Permian by the subduction of ancient Pacific Ocean floor [*Taira*, 2001]. Since the Miocene [*Nakamura et al.*, 1984], the Philippine Sea Plate is subducted beneath the Eurasian Plate at the Nankai subduction zone off the coast of SE Japan. Presently, the Philippine Sea Plate moves to the northwest with a convergence rate of ~4 cm a^{-1} [*Seno et al.*, 1993]. Sediments of the Shikoku Basin, forming the northwestern edge of the Philippine Sea Plate, are partially accreted to the front of the 100 km wide Nankai accretionary wedge in a series of fault-fold packets [*Park et al.*, 2002b] southeast of Shikoku Island (Figure 1a). Further upslope and landward of the zone of frontal accretion there is an important out-of-sequence megasplay fault branching off the plate boundary thrust at depth (Figure 1b) [e.g., *Park et al.*, 2002a; *Baba et al.*, 2006; *Wang and Hu*, 2006; *Tobin and Kinoshita*, 2006; *Moore et al.*, 2007]. Horizontal and vertical offset is at least 1250 m and 750 m, respectively [*Moore et al.*, 2009]. The fault zone is thought to be weak [*Park et al.*, 2002b], prone to seismic reactivation, and transferring displacement near to the seafloor [*Moore et al.*, 2007]. The megasplay fault lies in the coseismic rupture area of the 1944 Tonankai earthquake (M 8.0) and the 1946 Nankaido earthquake (M 8.1) [*Park et al.*, 2002a; *Baba and Cummins*, 2005; *Baba et al.*, 2006] and, thus, may have initiated historic tsunamis [*Park et al.*, 2002a; *Wang and Hu*, 2006; *Kimura et al.*, 2011]. During IODP Expeditions 314, 315, 316, 319, 322, 326, 332, 333, and 334, a transect of 12 sites (and multiple holes) were drilled on the Kumano transect perpendicular to the trench axis and across the accretionary prism and incoming plate (Figure 1a) [*Park et al.*, 2000; *Baba and Cummins*, 2005].

Table 1. List of Investigated Samples[a]

Core Number	333-C0012C-4H-5		333-C0011D-2H-2	316-C0007C-7X-1			316-C0006E-8H-1		316-C0006E-20X-2		316-C0008C-7H-8		316-C0008A-9H-3			316-C0004C-8H-2		315-C0001E-11H-1	
Experimental Subsample	K022		K020	K011	K012	K016	K007	K009	K013	K019	K015	K018	K002	K006	K014	K004	K010	K003	K005
Depth (mbsf)	**28.9**		**33.1**	62.8	62.8	62.8	48.2	48.2	127.9	127.9	60.9	60.9	76	76	76	65.2	65.2	90.6	90.6
Lithology	**hemipelagic/ pyroclastic clay, silty clay, and clayey silt**		**hemipelagic/ pyroclastic sediments, ash**	olive gray fine-grained sand			black fine-grained sand		fine grained sand, silty sand, and silty clay		silty clay		silty clay			silty clay		silty clay, clayey silt, and volcanic ash	
Characterization	**hemipelagic/ pyroclastic facies**		**hemipelagic/ pyroclastic facies**	trench wedge			sand-dominated trench wedge		mixed sand-mud trench wedge		slope basin sediments		slope basin sediments			slope-apron facies		slope-apron facies	
Quartz (%)	**20**		**8**		27		25.8		26.5		24.8		30.2			20.7		19.4	
Plagioclase (%)	**17**		**30**		36		29.4		23.3		29.6		21.7			15.9		18.1	
Calcite (%)	**0**		**0**		0		0.2		0		0.4		4.4			17.3		16.9	
Total clay (%)	**63**		**62**		37		44.6		50.2		45.2		43.7			46.1		45.7	

[a]Core numbers and experimental subsample numbers are given. The data are taken from *Expedition 315 Scientists* [2009], *Expedition 316 Scientists* [2009a, 2009b, 2009c, 2009d]. Data in bold type are taken from *Expedition 333 Scientists* [2012a, 2012b].

The water depths are between ~2500 and ~4100 m at the drill sites. In this study we focus on seven drill sites, from which we investigated a suite of nine whole round samples from a depth range between 28.9 and 127.97 mbsf (meters below seafloor; Table 1). Samples of the accretionary prism were collected during IODP Expedition 315 (Site C0001), Expedition 316 (Sites C0004, C0006, C0007, and C0008), and from the incoming Philippine Sea Plate during Expedition 333 (Sites C0011 and C0012, Figure 1a).

The following characterizations of IODP Sites C0011 and C0012 follow *Expedition 333 Scientists* [2012a, 2012b], and those of the accretionary prism sites (IODP Sites C0001, C0004, C0006, C0007, and C0008) follow *Expedition 315 Scientists* [2009] and *Expedition 316 Scientists* [2009a, 2009b, 2009c, 2009d].

The most seaward drill Site (C0012) is located on the incoming Philippine Sea Plate. Hemipelagic/pyroclastic clay, silty clay, and clayey silt of Unit I (Holocene to Miocene) are deposited above sandy volcanic turbidites of Unit II (upper Miocene). The sample investigated in this study (C0012C-4H-5, 28.9 mbsf, experimental subsample K022) belongs to Subunit IA.

Five lithological units were identified during IODP Expedition 322 at Site C0011. Later, the uppermost two units were the drilling target of IODP Expedition 333 at Site C0011. Unit I consists of hemipelagic/pyroclastic sediments (Holocene to upper Miocene), and Unit II is characterized as volcanic turbidite facies, dominated by tuffaceous sandstone, gravel, and sand beds (late Miocene). The sample investigated in this study (C0011D-2H-2, 33.1 mbsf, experimental subsample K020) belongs to Subunit IA.

IODP Sites C0007 and C0006 are located at the frontal thrust zone (accretionary prism toe). Four units were identified at Site C0007. Unit I is formed by Pleistocene fining-upward cycles of silty clay, sand, and silty sand. Based on a coarsening-upward trend of silt, sand, and gravel, Unit II is subdivided into four Subunits. Unit III is formed by Pliocene clay and silty clay with ash content. The boundary of Unit III and Unit IV is defined by a thrust fault and the occurrence of sand (possibly of Pleistocene age). The sample investigated in this study belongs to Subunit IIA (C0007C-7X-1, 62.89 mbsf, experimental subsamples K011, K012, and K016). Bedding planes were observed in subsample K012 (10 to 15° dip). Particle size analyses of this core section indicate 75% clay, 20% fine silt, and 5% medium silt [*Stipp et al.*, 2013].

Site C0006 is located landward of Site C0007 but still in the frontal thrust zone. Three lithological units were defined. Unit I is characterized as trench to slope transition facies formed by structureless Pleistocene clay. Unit II sediments are trench deposits of Pleistocene age.

Generally, the sand and silt content increases upward in Unit II. Unit III consists of Pleistocene to late Miocene silty clay with intercalated tuff layers. The sequence is interpreted as hemipelagic deep marine basin sediments. Two core samples from Site C0006 were investigated, both representing trench deposits: sample C0006E-8H-1 (48.23 mbsf, Subunit IIA, experimental subsamples K007 and K009) and sample C0006E-20X-2 (127.97 mbsf, Subunit IIB, experimental subsamples K013 and K019). Particle size analyses of core section C0006E-8H-1 indicate 85% clay, 10% fine silt, and 5% medium silt, and for core section C0006E-20X-2 60% clay, 30% fine silt, and 10% medium silt [*Stipp et al*., 2013].

Drilling at IODP Site C0008 recovered slope basin sediments seaward of the megasplay fault, i.e., in its footwall. Two lithological units were defined. Unit I is of Pleistocene to Pliocene age, with two subunits of silty clay, separated by the occurrence of mudclasts. The sand-rich turbidites of Unit II (Pliocene) are formed of pebbly sandstone with silty clay interbeds. Two samples from Site C0008 were investigated: sample C0008A-9H-3 (76.06 mbsf, experimental subsamples K002, K006, and K014) and C0008C-7H-8 (60.96 mbsf, experimental subsamples K015 and K018), both belonging to Unit I. Two aggregates of oxidized pyrite and some millimeter-sized white spots (possibly calcareous aggregates or shell fragments) at the surface and the sidewalls of the sample cylinder were observed during preparation. Sample C0008C-7H-8 contained a coarse-grained sand layer dipping with ~15° representing bedding (subsample K018). This sample showed several horizontal and vertical cracks. Both samples are similar in their particle size distribution of 75% clay, 20% fine silt, and 5% medium silt [*Stipp et al*., 2013].

Site C0004 is located ~1 km landward of Site C0008 in the immediate hanging wall of the megasplay fault. Four lithological units were identified. Unit I (Pleistocene) is a slope-apron facies, formed by silty clay with up to 25% nannofossils. Unit II (Pliocene) is subdivided in two subunits, a mass transport deposit (Subunit IIA) and silty clays (Subunit IIB). The upper and lower boundaries of the volcanic ash-bearing Unit III are marked by age reversals. The silty clays of Unit IV are characterized as underthrust slope facies. The analyzed sample (C0004C-8H-2, 65.26 mbsf, experimental subsamples K004 and K010) belongs to Unit I. Particle size analyses indicate 60% clay, 30% fine silt, and 10% of medium silt [*Stipp et al*., 2013].

Site C0001 is the most landward one investigated in this study. Two lithologic units were defined at this site. Unit I with three subunits is made up of silty clay, clayey silt, and volcanic ash layers in slope-apron facies of Quaternary to late Pliocene age. The boundary to Unit II is formed by an unconformity. The upper accretionary prism sediments of Unit II (late Pliocene to late Miocene age) are dominated by bioturbated silty clay to clayey silt. The sample investigated in this study (C0001E-11H-2, 90.6 mbsf, experimental subsample K003 and K005) belongs to Subunit IA. Particle size analyses indicate 60% clay, 30% fine silt, and 10% medium silt [*Stipp et al*., 2013].

3. Methods

Sonic travel times were measured during pressurization and triaxial deformation tests on the sample material. Only sections of whole round cores that were classified as undisturbed in computer tomography (CT) inspection aboard D/V *CHIKYU* were used to minimize errors caused by cracks and sample disruption. For the triaxial tests, we used a modified Moser Systemtechnik deformation apparatus at Kiel University with a maximal axial load of 10 kN and a maximal confining pressure (σ_3) of 1000 kPa (Figure 2). The apparatus is equipped with axial load, cell pressure, and displacement transducers, a pore pressure (σ_{pore}) and back pressure (σ_{back}) controlling system, a computer for operation and data acquisition, and Global Digital Systems Ltd bender elements mounted to the upper and lower pistons. The piezoelectric bender elements induce the sonic signal (a sine wave with a frequency of 5 kHz, and 10 kHz in experiment K022), and vice versa, they produce the electrical signal as a receiver. Displacement is generated in our experiments by the stepper motor (Figure 2) slowly moving the lower piston upward. The displacement transducers are capable to measure with 0.5 μm accuracy and thus with a negligibly small error.

Cylindrical samples of 50 mm in diameter and 48–102 mm in length prepared from the IODP drill cores were resaturated and pressurized in the triaxial deformation apparatus. Sonic measurements from the pressure increase stage after saturation as well as from the deformation stage of the experiments will be presented in this study. Deformation was carried out in three different types of geotechnical tests: (1) single step compression tests at constant confining pressure of 1000 kPa and constant displacement rates of 0.01 or 0.1 mm/min, (2) pressure

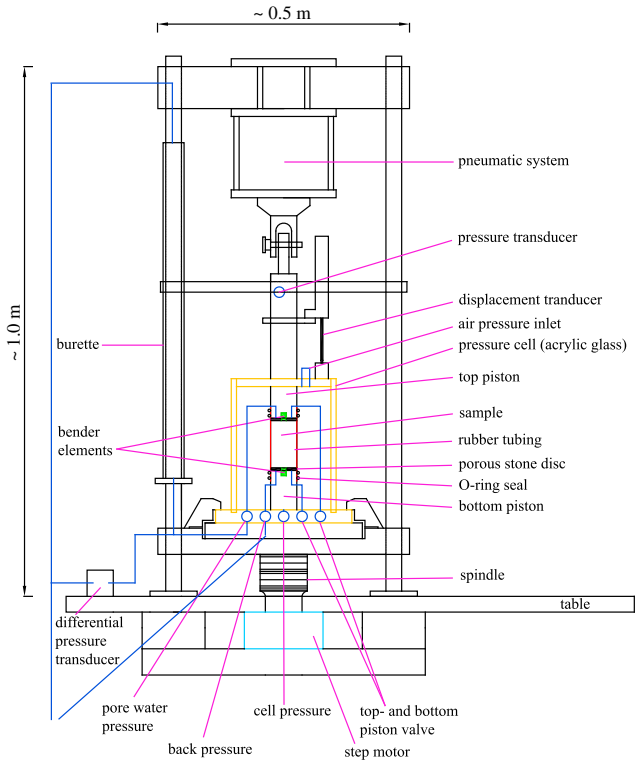

Figure 2. Schematic chart of the deformation apparatus from Moser Systemtechnik used for the triaxial deformation experiments (modified after M. Rolfs, unpublished manuscript, 2010).

stepping tests at constant displacement rates of 0.01 or 0.1 mm/min and stepwise increasing confining pressure (400 kPa, 640 kPa, and 1000 kPa) in three different deformation steps, and (3) rate stepping tests at constant confining pressure of 1000 kPa and stepwise increasing displacement rate in the range between 0.01 mm/min and 9 mm/min. Further information on the deformation apparatus, the experimental procedures, stress/strain and pore pressure/strain-diagrams, and plots of V_p, V_s, and displacement versus time are given in Figures S1–S3 and Text S1 in the supporting information.

Porosities of the drilled cores were initially determined by onboard pycnometer measurements (Table 2) [*Expedition 316 Scientists*, 2009e]. Changes in the sample porosities during experimental testing were calculated for the stages of pressure increase based on the expelled pore water (Table 2). This expelled pore water in the burette (Figure 2) could be measured with an accuracy of 0.075 ml for 50 ml pore water. During experimental deformation, the pore space is assumed to be constant since the deformation stages were conducted under undrained conditions. The density of the samples was determined after the triaxial deformation tests using a helium pycnometer with an error of ~0.2% (Quantachrome Corporation, 2011–2013). The error might be slightly increased due to effects caused by small pore radii in the fine-grained samples. To keep this error as low as possible, we purged the samples inside the sample chambers using helium with a pressure of 1.8 bars for up to 5 min. To control the density measurements, a sample with known density was measured during each analytical run in varying sample chambers. The sample mass was determined using a high-precision balance.

Table 2. Expelled Pore Water and Porosity Changes During the Phases of Pressure Increase During the Experiments[a]

Sample	Location	Depth (mbsf)	Density Beg. (g/cm^3)	Density End (g/cm^3)	Porosity Beg. (%)	Expelled Pore Water (mL)	Porosity End (%)	ΔPorosity
K020	IP	33.1	1.72	1.84	64.00	18.70	58.92	5.08
K022	IP	28.9	1.46	~2.1	72.00	33.00	49.13	14.87
K007	T	48.2	1.84	2.31	48.90	10.50	42.69	5.51
K009	T	48.2	1.84	2.11	48.90	16.50	39.60	8.60
K011	T	62.8	1.62	2.23	51.64	13.20	44.96	6.68
K012	T	62.8	1.62	2.15	51.64	10.00	46.90	4.74
K016	T	62.8	1.62	2.20	51.64	3.80	49.70	1.94
K013	T	127.9	1.89	2.0	47.70	10.40	41.57	6.13
K019	T	127.9	1.89	1.99	47.40	9.80	42.10	5.30
K015	FW	60.9	1.73	2.08	56.79	12.90	50.31	6.48
K018	FW	60.9	1.73	2.01	56.79	8.00	52.78	4.01
K002	FW	76.0	1.87	nv	52.19	9.60	47.21	4.98
K006	FW	76.0	1.87	2.01	52.19	4.00	50.02	2.17
K014	FW	76.0	1.87	1.9	52.19	14.30	44.13	8.06
K003	HW	90.6	1.6	1.85	61.73	14.80	55.83	5.90
K010	HW	65.2	1.7	1.8	63.82	24.30	54.50	9.32

[a]No pore water measurements are available for experiments K004 and K005. Porosity and density data of the beginning (beg.) are taken from *Expedition 315 Scientists* [2009], *Expedition 316 Scientists* [2009a, 2009b, 2009c, 2009d], and *Expedition 333 Scientists* [2012a, 2012b]. IP = incoming plate, T = accretionary prism toe, FW = footwall of the megasplay fault, HW = hanging wall of the megasplay fault.

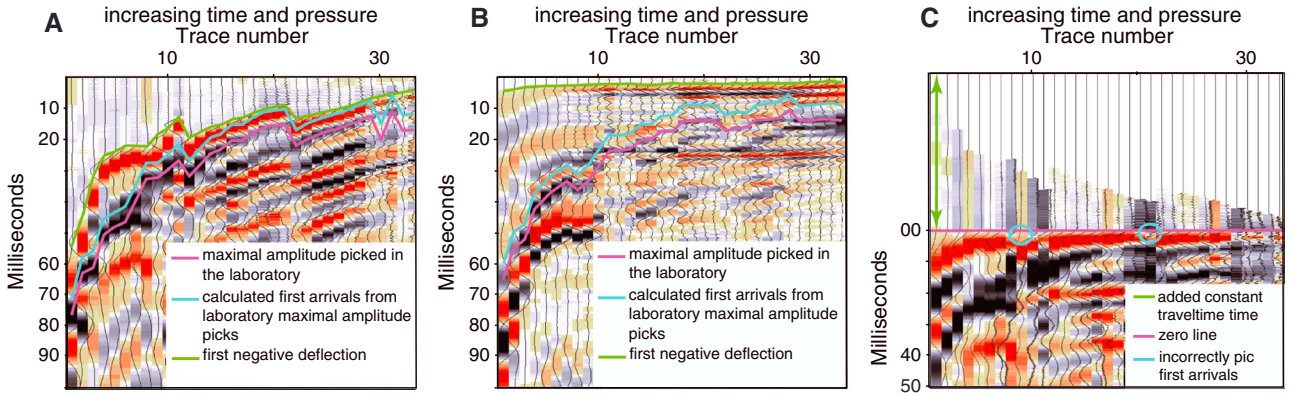

Figure 3. Data example to illustrate the picking and processing procedures. The wave records were color coded for better first arrival detection. Negative deflections are shown in red; positive deflections in black. (a) Shear test gather of the *S* wave recorded from sample K016. Single trace measurements conducted during the triaxial deformation experiments are aligned (*x* axis) to clarify variations in the travel time of the acoustic waves (*y* axis). For first data evaluation, maximum amplitudes were picked in the laboratory (purple line). Half the length of the transmitted signal was subtracted from the maximum amplitude to identify the first arrivals (blue line). Sorting the data into common shear test gathers and color-coding helped to identify correct first arrivals. First arrivals are handpicked during reprocessing (green line). (b) Shear test gather of the *P* waves of sample K016. Maximum amplitudes picked in the laboratory (purple line) can be identified as multiples by sorting into the shear test gather. Handpicked first arrivals are indicated by a green line. (c) Application of a static correction to the identified first arrivals, to minimize picking errors. A theoretical constant travel time (green line) was added to the data, and the previously picked first arrival travel time was subtracted. This ideally projects the first arrivals into a straight line (zero line, purple). A mismatch of the first negative deflection and the purple line is indicative for erroneous first arrival picking (blue circles). After correction of erroneous picks, the travel time manipulations were reversed and sonic velocities were recalculated.

Sonic velocity measurements were performed using bender elements capable of generating both, compression waves (*P* waves) and shear waves (*S* waves). The resulting wavelength is 30 cm (for V_p of 1500 m/s) and 6 cm (for V_s of 300 m/s) in case of 5 kHz and 15 cm and 3 cm in case of 10 kHz. For the *P* waves, this results in a wavelength of up to 5 times the sample length. For the *S* waves the wavelength is much shorter due to lower V_s. As a result, we were not able to interpret the wavelet after the first arrival, since it is influenced by interference and extinction of the transmitted signal, reflected and converted signals from the sidewalls, multiples, and noise. For this reason, frequency and amplitude of the signal cannot be analyzed. However, the first arrivals were useable, and after data processing, we were able to reliably identify first arrivals. A vertical wave path parallel to the core axis was chosen. Compressional (V_p) and shear (V_s) wave velocities were calculated from the travel times and the sample lengths. The most important uncertainties in velocity measurements are caused by the quality of the receiver signal [e.g., *Leong et al.*, 2005], which depends on the specimen-transducer coupling and the noise produced by the shear apparatus. To optimize coupling, *Dyvik and Madshus* [1985] introduced plate-like bender elements. The prismatic end faces of the bender elements extend into the specimen, ensuring an optimal soil transducer coupling [*Lee and Santamarina*, 2005].

During the initial pressure increase, V_p and V_s measurements were conducted in ~100 kPa steps, except for experiments K020 and K022, for which the velocities were measured in time steps of ~60 s. During the deformation stages, V_p and V_s were determined in axial strain intervals of ~2 to 3%, except for the fast rate stepping tests. In experiments K020 and K022, we performed six velocity measurements in time steps of ~300 s. The number of sonic velocity measurements are in the range between three and ten measurements per deformation stage (dependent on strain), resulting in 15 to 39 sonic velocity measurements for each experiment including the pressurization stage, except for experiments K020 (~1220 *P* and *S* wave measurements) and K022 (~ 600 *P* and *S* wave measurements).

The travel time measurements are a source of error, since reflection and refraction at the side walls can cause interference of the waves [*Leong et al.*, 2005]. Several methods for travel time determination have been proposed; nevertheless, the derived velocities are similar [e.g., *Viggiani and Atkinson*, 1995; *Santamarina and Fam*, 1997; *Leong et al.*, 2005]. We used first arrival picking [*Viggiani and Atkinson*, 1995; *Arulnathan et al.*, 1998]. *Leong et al.* [2005] report on different methods for the identification of the first arrivals: (a) first deflection of the receiver signal and (b) first reversal point of the receiver signal. We used the first negative deflection as first arrival in our study. The high sampling rate (1 MHz) ensured good data resolution, and we were able to identify this point with high accuracy by color coding of the wavelet (Figure 3). The picking error is estimated to be 0.0015 ms and 0.003 ms for the *P* and the *S* waves, respectively. This results in velocity errors between 3 and 10%, depending on the travel time. We conducted two reference studies (K020 and K022) with high data redundancy to eliminate potential errors in the velocity measurements.

No temperature correction was applied, since absolute velocity changes are minor for a temperature rise from 10 to 100°C [*Bourbié et al*., 1987]. A V_p decrease of 1.7% and a V_s decrease of 0.9% was determined for a temperature rise of 100°C [*Timur*, 1977]. The temperature in the laboratory was held at 20–22°C, while downhole temperatures in the drill holes range between 3.2°C (316-C0006E-8H-1) and 5.5°C (316-C0006E-20X-2) [*Expedition 316 Scientists*, 2009b]. Thus, the temperature difference would cause an estimated error of ~0.25% (V_p) and ~0.13% (V_s), respectively.

For data analysis, we allocated *P* and *S* wave pairs into common shear test gathers to identify misfits of manual first arrival time picks. For first data analysis in the laboratory, we picked the maximum amplitude of the first recorded signal and subtracted half the length of the transmitted signal to determine the first arrivals. This method has several potential sources of errors. First, the length of the transmitted and the received signal is not identical, caused by attenuation and distortion [*Arulnathan et al*., 1998; *Leong et al*., 2005]. The length of the received signal decreases with increasing principal stress (σ_1) due to increased grain-grain contacts and decreased damping and, thus, leads to systematic misinterpretation of the first arrivals (Figures 3a and 3b). Second, picking of the maximal amplitude occasionally leads to detection of multiple and converted signals as well as to detection of *S* waves produced by the side lobes of the bender elements or by poor soil-transducer coupling (especially in case of *P* wave measurements). Multiple, converted, and reflected signals such as reflection and refraction from the sample boundary [*Leong et al*., 2005] occasionally cause a misinterpretation of the first arrivals. According to *Lee and Santamarina* [2005] and *Leong et al*. [2005], especially reflected *P* waves may interfere with direct *S* waves resulting in an overestimation of V_s. Therefore, filters were used to eliminate noise, produced by the side lobes of the bender elements and by the deformation apparatus.

Reprocessing of the data was carried out using the Omega 2 software (WesternGeco–Schlumberger). Seismic time series analysis helped to identify primary, multiple, and reflected signals, especially *P* waves generated at the side lobes of the bender element [*Santamarina and Fam*, 1997]. The data are presented as color-coded wiggle plots (Figures 3a and 3b) enabling an easy identification and control of the first arrivals. The static correction (Figure 3c) comprises a second quality check. For this, we add a constant travel time value to the measured travel time and then subtract the initial first arrival times. This projects the first arrivals ideally into a straight line and enables easy checking of the picked arrivals (first arrivals should then lie in a zero line in Figure 3c). After checking of the arrivals, we reverse the travel time manipulations and recalculate the wave velocities. This procedure guaranteed good quality first arrival detection.

Mechanical and petrophysical properties can be determined by measuring compression wave and shear wave velocities (V_p and V_s). From the following equations we calculated the shear and bulk modulus:

$$Vp = \sqrt{\left(\kappa + \frac{3}{4}\mu/\rho\right)} \tag{1}$$

and

$$Vs = \sqrt{(\mu/\rho)} \tag{2}$$

where μ is the shear modulus, κ is the bulk modulus, and ρ is the density. From the shear and bulk moduli we calculated the elastic modulus E according to the following equation:

$$E = 9\kappa\mu/3\kappa + \mu \tag{3}$$

The equations assume isotropy of the sample material. The effect of anisotropy on sonic velocity [e.g., *Johnston and Christensen*, 1993], however, cannot be neglected for our study, because we used naturally compacted samples as starting material and these samples were deformed up to a maximum axial shortening strain of ~64%. We therefore come back to this topic in the discussion.

4. Results

4.1. Porosity and Density

Shipboard measurements [*Expedition 315 Scientists*, 2009; *Expedition 316 Scientists*, 2009a, 2009b, 2009c, 2009d] indicate that porosities decrease with sediment depth (Table 2) ranging between 72% (333-C0011D-2H-2) and

Table 3. Overview of the Experiments[a]

Sample	Core Section	Type	Experimental Conditions	Axial Strain
K002	316-C0008A-9H-3	constant strain rate	confining pressure: 1000 kPa displacement rate: 0.01 mm/min	12%
K003	315-C0001E-11H-1	constant strain rate	confining pressure: 1000 kPa displacement rate: 0.01 mm/min	36%
K004	316-C0004C-8H-2	pressure stepping	confining pressure: 400 kPa,, 640 kPa, and 1000 kPa displacement rate: 0.01 mm/min	first step: 10% second step: 14% third step: 37%
K005	315-C0001E-11H-1	pressure stepping	confining pressure: 400 kPa, 640 kPa, and 1000 kPa displacement rate: 0.01 mm/min	first step: 13% second step: 17% third step: 40%
K006	316-C0008A-9H-3	constant strain rate	confining pressure: 1000 kPa displacement rate: 0.1 mm/min	31%
K007	316-C0006E-8H-1	constant strain rate	confining pressure: 1000 kPa displacement rate: 0.01 mm/min	22%
K009	316-C0006E-8H-1	pressure stepping	confining pressure: 400 kPa, 640 kPa, and 1000 kPa displacement rate: 0.01 mm/min	first step: 41% second step: 46% third step: 61%
K010	316-C0004C-8H-2	velocity stepping	confining pressure: 1000 kPa displacement rate: 0.5 mm/min, 1.0 mm/min, 5.0 mm/min, and 9.0 mm/min	first step: 16% second step: 19% third step: 23% fourth step: 44%
K011	316-C0007C-7X-1	pressure stepping	confining pressure: 400 kPa, 640 kPa, and 1000 kPa displacement rate: 0.01 mm/min	first step: 19% second step: 22% third step: 42%
K012	316-C0007C-7X-1	velocity stepping	confining pressure: 1000 kPa displacement rate: 0.5 mm/min, 1.0 mm/min, 5.0 mm/min, and 9.0 mm/min	first step: 14% second step:21% third step: 25% fourth step: 36%
K013	316-C0006E-20X-2	pressure stepping	confining pressure: 400 kPa, 640 kPa, and 1000 kPa displacement rate: 0.01 mm/min	first step: 17% second step: 24% third step: 42%
K014	316-C0008A9H-3	pressure stepping	confining pressure: 400 kPa, 640 kPa, and 1000 kPa displacement rate: 0.01 mm/min	first step: 20% second step: 27% third step: 43%
K015	316-C0008C-7H-8	pressure stepping	confining pressure: 400 kPa, 640 kPa, and 1000 kPa displacement rate: 0.01 mm/min	first step: 9% second step: 12% third step: 19%
K016	316-C0007C-7X-1	pressure stepping	confining pressure: 400 kPa, 640 kPa, and 1000 kPa displacement rate: 0.01 mm/min	first step: 15% second step: 20% third step: 38%
K018	316-C0008C-7H-8	velocity stepping	confining pressure: 1000 kPa displacement rate: 0.01 mm/min, 0.05 mm/min, and 0.1 mm/min	first step: 19% second step: 24% third step: 28%
K019	316-C0006E-20X-2	velocity stepping	confining pressure: 1000 kPa displacement rate: 0.01 mm/min, 0.05 mm/min, 0.1 mm/min, 0.5 mm/min, 0.5 mm/min, and 1.0 mm/min	first step: 16% second step: 20% third step: 23% fourth step: 26% fifth step: 29% sixth step: 46%
K020	333-C0011D-2H-2	pressure stepping	confining pressure: 400 kPa, 640 kPa, and 1000 kPa displacement rate: 0.01 mm/min	first step: 6% second step: 13% third step: 19%
K022	333-C0012C-4H-5	pressure stepping	confining pressure: 400 kPa, 640 kPa, and 1000 kPa displacement rate: 0.01 mm/min	first step: 8% second step: 13% third step: 37%

[a]The type of triaxial shear test and the strain rates of the single deformation phases are given in the table.

64% (333-C0012C4H-5) for the incoming plate, between 48.9% (316-C0007C-7X-1) and 47.7% (316-C0006E-20X-2) for the prism toe, between 56.8% (316-C0008C-7H-8) and 52.2% (316-C0008A-9H-3) for the footwall of the megasplay fault, and between 63.8% (316-C0004C-8H-2) and 61.7% (315-C0001E-11H-1) for the hanging wall of the megasplay fault. The only exception to this trend is observed for the samples from core segment 316-C0007C-7X-1 (K011, K012, and K016) which show higher porosities of 62.8% compared to shallower sediments (48.2%, K007 and K009). The bulk density of the samples increases with sediment depth as well, with a few exceptions. The bulk density of core segment 316-C0007C-7X-1 (1.62 g/cm^3) is less than for the shallower

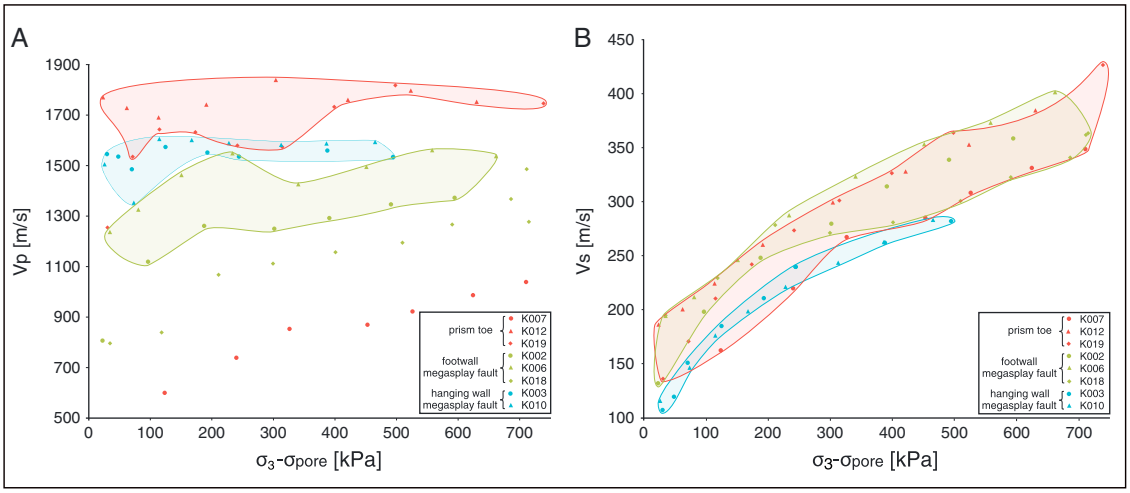

Figure 4. Plots of the values for (a) V_p and (b) V_s versus the effective confining pressure (σ_3-pore water pressure) measured during the stage of confining pressure increase (from 300 to 1000 kPa) in the single-step compression tests and the rate stepping tests. The low velocities recorded for sample K007 and the first data points of K002 and K019 are related to poor sample-transducer coupling. Low velocities in sample K018 are related to incomplete sample saturation.

sediments of core segment 316-C0006E-8H-1 (1.84 g/cm^3); both come from the prism toe area. The same is observed for the densities of the hanging wall sediments, where the density decreases with depth from 1.7 g/cm^3 in 65.2 mbsf (316-C0004C-8H-2) to 1.6 g/cm^3 in 90.6 mbsf (316-C0001E-11H-1). During pressurization, bulk density of the samples is increased and ranges between 1.8 and 2.3 g/cm^3 after completion of the experiments (Table 2). The estimated porosity losses during the experiments are in the range between 1.94% (K016) and 14.87% (K022). The porosity loss depends on the initial porosity, the pressurization, the fabric, and other factors. No trend for the different drill sites and tectonic settings could be determined. A detailed overview of the amounts of expelled pore water and the resulting porosity changes is given in Table 2.

4.2. Velocity Data

In the following section, we describe the results of the *P* and *S* wave velocity measurements arranged in diagrams for the different types of test. Data points are marked for the different tectonic settings and are described along the IODP cross section (Figure 1) in direction toward the coast.

4.2.1. Stage of Pressure Increase

This stage comprises the phases of pressure increase ($\sigma_1 = \sigma_3$) subsequent to the sample saturation and also between the deformation steps of the pressure stepping tests. For single-step compression tests and rate stepping tests, we increased $\sigma_1 = \sigma_3$ from 300 to 1000 kPa. For the pressure stepping tests, we increased $\sigma_1 = \sigma_3$ in three steps from 300 to 400 kPa, from 400 to 640 kPa, and from 640 to 1000 kPa (Table 3). These stages of confining pressure increase were carried out under consolidated drained conditions.

In the single-step compression tests and the rate stepping tests, *P* wave velocities are more or less constant or display only a slight increase for some of the samples with increasing effective confining pressure (Figure 4a). Samples from the accretionary prism toe (K012 and K019; Figure 4a) have the highest values of V_p ranging between ~1550 m/s and ~1800 m/s except for sample K007 and the first data point of sample K019. This sample displays unrealistically low V_p values below V_p in water (between ~600 and ~1040 m/s, and 1250 m/s, respectively) which was probably caused by incomplete coupling between bender elements and sample surface. Therefore, we have not interpreted the results of K007 and the first data point of K019 any further.

Samples K002 and K006 from the megasplay footwall show V_p values ranging between ~1100 m/s and ~1560 m/s except for one unrealistically low data point of ~800 m/s (Figure 4a), may be caused by incomplete coupling at the given low effective confining pressure. Low starting values of V_p could generally be caused by this effect. A third sample from the same setting (K018) was the only sample in which the pore water content has been proven to be not fully saturated (see Figure S1). That is why we exclude this sample from any further interpretation. Also, sample K002 displays very low V_p values, but we have no evidence for undersaturated pore water conditions or missing coupling between sample and bender elements. Samples from the megasplay hanging wall (K003 and K010) are characterized by intermediate V_p values in the range between ~1350 m/s and ~1600 m/s (Figure 4a).

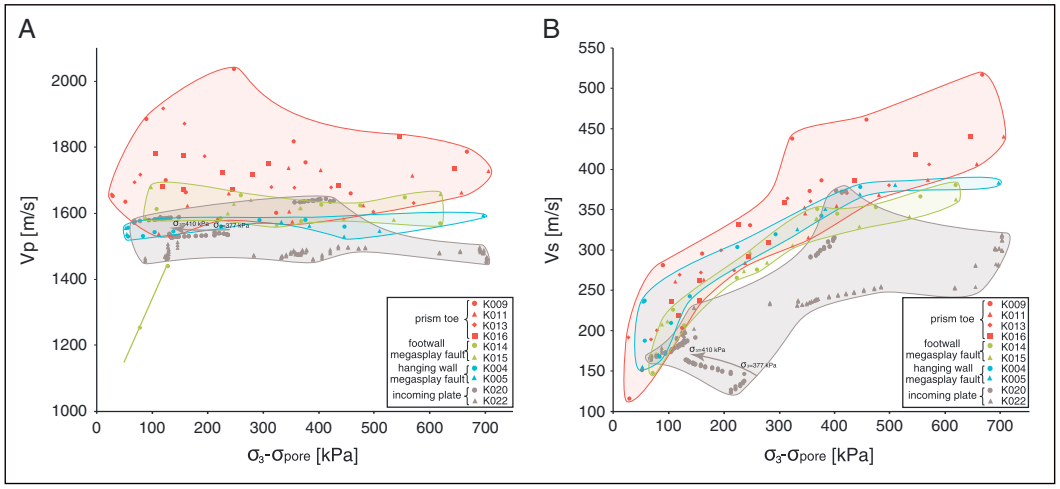

Figure 5. Plots of the values for (a) V_p and (b) V_s versus the effective confining pressure (σ_3-pore water pressure), recorded during the stages of confining pressure increase in the pressure stepping tests. Confining pressures were increased in three steps (300 to 400 kPa, 400 to 640 kPa, and 640 to 1000 kPa). During deformation intervals, the confining pressure was held constant. The strong increase in V_p recorded in sample K014 is attributed to poor sample-transducer coupling at low confining pressure. The grey arrow shows the evolution of V_p in experiment K020. In response to a strong deformation-related increase in pore water pressure, the effective (σ_3 decreases.

S wave velocities of the single step compression tests and the rate stepping tests show a significant and consistent increase with increasing effective confining pressure for all of the samples (Figure 4b). The highest velocity increase from ~136 m/s to ~430 m/s is observed for sample K019 from the accretionary prism toe. There is also no widespread for the different tectonic settings, but the V_s values of the different samples are rather similar at the same effective confining pressure ranging within 100 m/s and mostly around 50 m/s (Figure 4b).

In the pressure stepping tests, we also observed a rather constant V_p for the three stages of pressure increase (Figure 5a). The samples from the incoming plate show the lowest V_p values ranging between ~1540 m/s and ~1640 m/s for sample K020 and between ~1455 m/s and ~1510 m/s for sample K022. A rather wide range of V_p is observed for the accretionary prism toe samples (K009, K011, K013, and K016). The lowest velocity was found in samples K011 (~1540 m/s), which overlaps with the data of the incoming plate sediments, while the majority of the V_p values of the prism toe are higher than the data from the other tectonic settings (Figure 5a). Samples from the megasplay footwall (K014 and K015) show relatively uniform velocities of ~1600 m/s except for two very low data points of 1250 m/s and 1440 m/s from sample K014 which might be caused by incomplete coupling between bender elements and sample surface at the given low effective confining pressures. These two data points are not further considered. The samples from the megasplay hanging wall (K004 and K005) display slightly lower V_p values of ~1550 m/s, and their spread is even smaller than for the footwall samples (Figure 5a).

V_s data of the pressure stepping tests are characterized by a clear increase with increasing effective confining pressure for the different tectonic settings (Figure 5b). The incoming plate samples (K020 and K022) generally show the lowest velocities ranging between ~130 m/s and ~380 m/s. The abnormal trend in K020 (first stage of pressure increase, marked by an arrow in Figure 5b) is caused by decreasing effective confining pressure due to strongly increasing pore water pressure. The samples from the accretionary prism toe (K009, K011, K013, and K016) display the highest velocities (Figure 5b). In sample K009, the velocity increases from ~115 m/s to ~520 m/s at the end of the third pressure increase. Intermediate velocities (between ~150 m/s and ~380 m/s) but significantly overlapping with the prism toe data set were observed for the samples from the megasplay footwall (K014 and K015) and from the megasplay hanging wall (K004 and K005). These velocity data spread only slighty for a specific effective confining pressure (Figure 5b).

4.2.2. Deformation Stage

The stage of deformation comprises all stages of increasing σ_1 while σ_3 is kept constant. In the single-step compression tests and the rate stepping tests, σ_3 was held constant at ~1000 kPa, while σ_1 was increased. During the pressure stepping tests, three deformation stages were carried out at $\sigma_3 = 400$ kPa, at $\sigma_3 = 640$ kPa, and at $\sigma_3 = 1000$ kPa (Table 3). Triaxial deformation was always carried out under consolidated-undrained conditions.

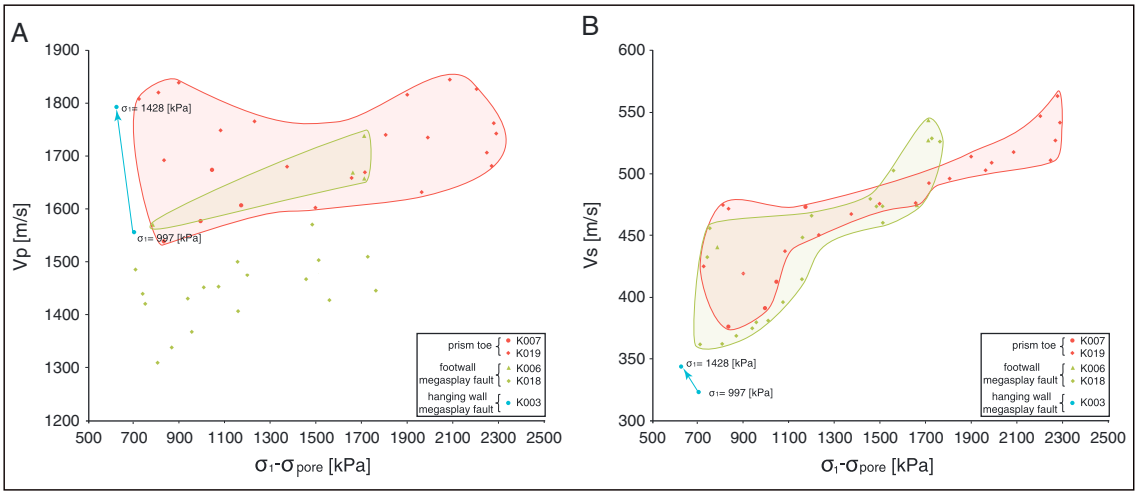

Figure 6. Plots of the values for (a) V_p and (b) V_s versus the effective axial stress (σ_1-pore water pressure) measured during the deformation stages of the single-step compression tests and the rate stepping tests. Both single-step compression tests and rate stepping tests were conducted at 1000 kPa confining pressure. The effective axial stress decrease observed in experiment K003 is due to a strong deformation-related increase in pore water pressure. Values for the increasing effective axial stress are indicated.

In the single-step compression tests and the rate stepping tests, V_p data are characterized by a widespread and a weak increase with increasing effective stress (Figure 6a). Samples from the accretionary prism toe (K007 and K019) show the highest velocities (~1540 m/s to ~1800 m/s), with velocities at high largest principal stress being slightly faster than those at low principal stress. V_p values from the megasplay footwall (K006) are lower (~1570 m/s and ~1700 m/s) overlapping with the prism toe velocities, and they increase also slightly toward largest principal stress (Figure 6a). The V_p data of sample K018 are not considered further in this data set due to uncertain sample saturation conditions. The data set from the megasplay hanging wall (K003) is too small for meaningful interpretation.

The available *S* wave velocities from the accretionary prism toe and the megasplay footwall largely overlap with a relatively small spread (Figure 6b). They become clearly higher with increasing effective stress ranging between ~360 m/s and ~560 m/s. The lowest V_s values between ~320 and ~340 m/s were measured for the hanging wall sample K003, which was only tested at low effective axial stress (Figure 6b).

Sonic velocity measurements conducted during the pressure stepping experiments indicate that there are rather constant or slightly increasing *P* wave velocities with increasing effective stress and a partial overlap of the four tectonic settings (Figure 7a). The data set displays a large spread for specific effective stresses. The

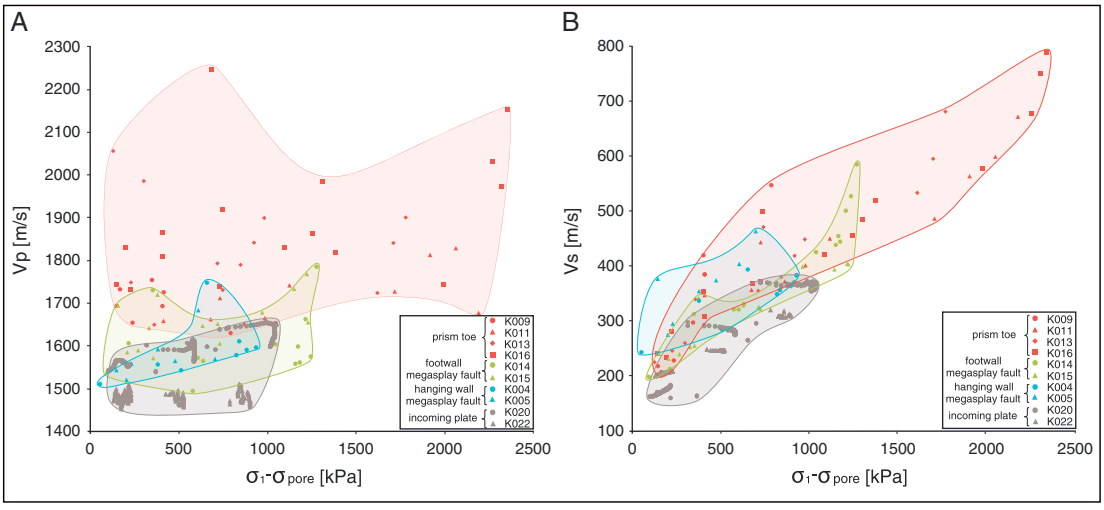

Figure 7. Plots of the values for (a) V_p and (b) V_s versus the effective axial stress (σ_1-pore water pressure) measured during the deformation stages of the pressure stepping tests. Between the deformation stages of the pressure stepping tests, confining pressure was increased stepwise from 300 to 400 kPa, from 400 to 640 kPa, and then from 640 to 1000 kPa.

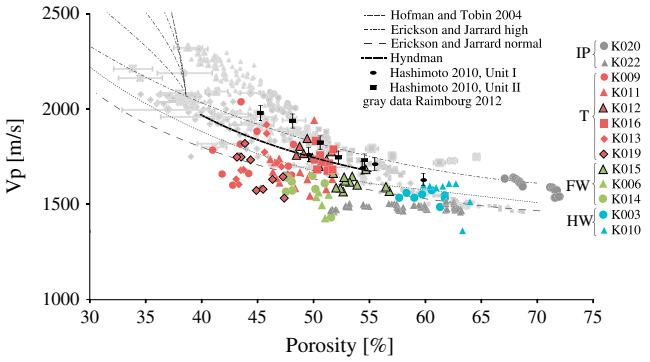

Figure 8. Compilation of V_p-porosity relationships in comparison to different published studies. A few data sets are not included, because they are unreliable due to poor sample-transducer coupling and incomplete pore water saturation (see text for further explanation). Porosity data were calculated from the initial porosity and the amount of expelled pore water. IP = incoming plate; T = accretionary prism toe; FW = footwall of the megasplay fault; HW = hanging wall of the megasplay fault. Compiled published data sets: *Raimbourg et al.* [2011] from IODP Sites C0001, C0002, C0006, and C0007 as well as from ODP Site 1173 from the Nankai accretionary prism (in grey); *Hashimoto et al.* [2010] from Site C0001 (in black); *Hoffman and Tobin* [2004] from the Shikoku Basin (ODP Site 1173) (dotted line); *Hyndman et al.* [1993] from ODP Site 808 at the outermost toe of the Nankai accretionary prism (thick dashed line); global velocity-porosity trend of *Erickson and Jarrard* [1998] for highly and normally consolidated sediments (thin dashed lines).

incoming plate sample K022 shows the lowest values for V_p of up to ~1500 m/s. The data of sample K020 overlap with those from the megasplay footwall and hanging wall samples. The highest velocities were measured in the sediments from the accretionary prism toe (K009, K011, K013, and K016), ranging between ~1660 m/s (K009) and ~2250 m/s (K016). Samples from the megasplay footwall (K014 and K015) and hanging wall (K004 and K005) are comparable and range between ~1540 m/s and ~1730 m/s (K015) at the end of the deformation (Figure 7a).

S wave velocities show a clear increase with increasing effective axial stress (Figure 7b). The trend of the entire data set is very clear with only a small spread. Data largely overlap and there is no clear difference in the V_s values between the four tectonic settings, with the exception of the two samples from the incoming plate (K020, K022), which show slightly lower velocities (V_s between ~160 m/s and ~360 m/s). Samples from the accretionary prism toe extend toward higher V_s and stress values. The highest V_s of ~790 m/s was measured at the highest effective stress (sample K016).

The reliable V_p data from the pressure increase stages are plotted against the porosity evolving under the drained conditions (Figure 8; porosities were calculated from the initial porosity and the amount of expelled pore water). Our data are compared to velocity-porosity data from other studies and different tectonic settings. A global V_p porosity relationship for highly and normally consolidated sediments based on Ocean Drilling Program data from Amazon Fan is proposed by *Erickson and Jarrard* [1998]. The empirical relationship of *Hoffman and Tobin* [2004] is derived from sediments of the Shikoku Basin (Ocean Drilling Program Site 1173). Data from *Hyndman et al.* [1993] were determined on sediments from the toe of the Nankai accretionary prism (Ocean Drilling Program Site 808). *Hashimoto et al.* [2010] measured also on samples from the hanging wall of the megasplay fault (IODP Site C0001). Further samples from the hanging wall of the megasplay fault (IODP Sites C0001 and C0002) and from the accretionary prism toe (IODP Sites C0006 and C0007) as well as from the Shikoku Basin (Ocean Drilling Program Site 1173) were analyzed by *Raimbourg et al.* [2011].

4.3. Shear Parameters

From the velocity data at σ_{1max} the shear modulus (μ) and the bulk modulus (κ) were calculated using equations (1) and (2). Moduli calculation was done for all samples yielding reliable velocity measurements, and results are given in Table 4. The two samples from the incoming plate have the lowest shear moduli of 0.20 GPa and 0.24 GPa. Shear moduli from the accretionary prism toe are the highest ranging between 0.52 GPa and 1.37 GPa. The sediments from the megasplay footwall display shear moduli between 0.32 GPa and 0.65 GPa and those for the megasplay hanging wall between 0.22 GPa and 0.30 GPa. Bulk moduli for the samples from the incoming plate range between 4.40 GPa and 4.42 GPa, from the accretionary prism toe between 4.94 GPa and 8.41 GPa, from the megasplay footwall between 3.85 GPa and 5.85 GPa, and from the megasplay hanging wall between 4.53 GPa and 5.67 GPa, (Table 4). The elastic modulus (E) is a direct measure of the stiffness of a material and can be determined from the shear and the bulk modulus using equation (3). The elastic moduli for the incoming plate samples range between 0.59 GPa and 0.69 GPa, from the accretionary prism toe between 1.5 GPa and 3.89 GPa, from the megasplay footwall between 0.95 GPa and 1.87 GPa, and from the megasplay hanging wall between 0.64 GPa and 0.88 GPa (Table 4).

Table 4. Shear, Bulk, and Elastic Moduli of the Samples[a]

Sample	Location	V_p (m/s)	V_s (m/s)	Density (g/cm^3)	Shear Modulus (GPa)	Bulk Modulus (GPa)	Elastic Modulus (GPa)
K020	IP	1598.60	357.07	1.84	0.24	4.40	0.69
K022	IP	1493.82	308.44	2.10	0.20	4.42	0.59
K007	T	1607.42	473.35	2.31	0.52	5.28	1.50
K011	T	1677.94	671.23	2.23	1.01	4.94	2.82
K016	T	2153.27	787.41	2.21	1.37	8.41	3.89
K013	T	1901.02	680.38	2.01	0.93	6.02	2.65
K019	T	1743.08	541.60	2.00	0.59	5.29	1.69
K015	FW	1733.92	393.26	2.09	0.32	5.85	0.95
K006	FW	1658.17	543.61	2.02	0.60	4.75	1.71
K014	FW	1785.73	584.35	1.90	0.65	5.20	1.87
K004	HW	1579.01	348.26	1.94	0.24	4.53	0.69
K003	HW	1793.25	343.97	1.85	0.22	5.67	0.64
K005	HW	1684.13	403.24	1.85	0.30	4.85	0.88

[a]Shear and bulk moduli are calculated using the wet bulk density and the velocity measured at σ_{1max} in the deformation experiments. The density of K022 is calculated from the sample volume and the sample mass subsequent to the triaxial testing. For samples K002, K009, K010, K012, and K018, no reliable velocity data were available. From the shear and bulk moduli, the elastic modulus was calculated. IP = incoming plate, T = accretionary prism toe, FW = footwall of the megasplay fault, HW = hanging wall of the megasplay fault.

5. Discussion

5.1. *P* Wave Velocities of Nankai Trough Sediments

Logging while drilling (LWD) data of Hole C0001D from the hanging wall of the megasplay fault [*Kinoshita et al*., 2009] are in good agreement to the V_p data of our samples from the same location and Hole C0004 measured during the pressure increase stage (see Figure 9). The V_p values from footwall and incoming plate samples are close to the LWD data of Hole C0001D, while samples from the accretionary prism toe deviate significantly and show consistently higher V_p values.

The V_p data of *Hashimoto et al*. [2010] on cores of Site C0001 from similar depth (1630–1710 m/s at 390–712 kPa effective confining pressure) are slightly higher than those determined in our study for the hanging wall (about 1530–1650 m/s; see Figures 5, 8, and 9), which is probably due to the slightly higher effective confining pressures in the study of *Hashimoto et al*. [2010]. The testing methods are also slightly different in the two studies, but differences in the velocities are small and within the range of experimental errors discussed above in section 3. Shikoku Basin sediment data of *Hoffman and Tobin* [2004] corrected for in situ conditions, data from ODP Site 808 under in situ pressure conditions [*Hyndman et al*., 1993], from Sites C0001, C0002, C0006, and C0007 as well as from ODP Site 1173 from isotropic loading tests extrapolated to in situ conditions [*Raimbourg et al*., 2011], show similar or slightly increased V_p values, if compared to our data (Figure 8). Lower values of our study result from variable confining pressure levels, lower than the in situ pressure conditions. A few very low velocity data points could also be caused by insufficient coupling between the bender elements and the samples. As has been pointed out before, this coupling problem does not occur during deformation at elevated principal stresses and hence elevated contact pressures indicating that it is likely induced by low effective confining pressure during the stage of pressure increase.

What becomes evident from the work cited above and from our data is that compressional wave velocities of fine-grained sediments from the hanging wall of the megasplay fault are similar or slightly higher than the values reported by *Shumway* [1960] for unconsolidated marine sediments ranging from shallow water sands to deep-sea clays and values from *Hamilton* [1970] and *Hamilton and Bachman* [1982] for near-mudline, water-saturated sediments from the Northern Pacific. Since diagenetic effects like cementation can be excluded in our samples, we infer that most if not all of the changes in the acoustic velocities are caused by fabric changes in response to consolidation and/or natural or experimental deformation and by compositional differences. Shape and crystallographic preferred orientation analysis indicates that samples from the topmost sedimentary sequence down to 128 mbsf show already a preferred alignment of the clay minerals [*Milliken and Reed*, 2010; *Saffer et al*., 2011; *Raimbourg et al*., 2011; K. Schumann, Texture development in naturally compacted and experimentally deformed silty clay sediments from the Nankai Trench, Japan (NanTroSEIZE, IODP Expeditions 315, 316, 333), submitted to *Tectonophysics*, 2013].

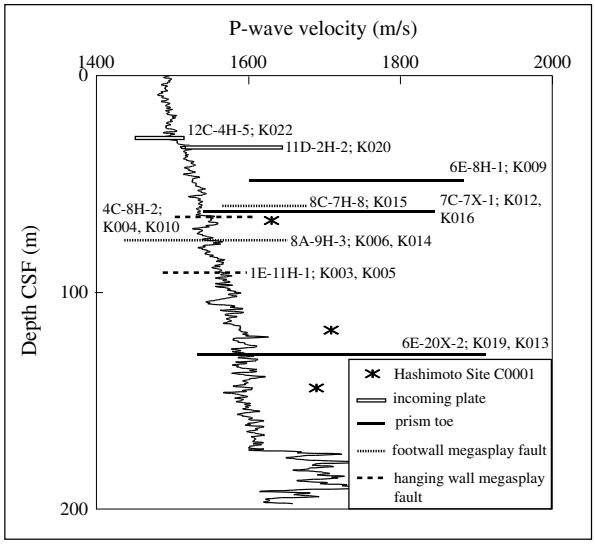

Figure 9. Logging while drilling *P* wave velocity measurements of Expedition 315 Site C0001D from *Expedition 315 Scientists* [2009] in comparison to V_p data from this study and from *Hashimoto et al.* [2010]. The megasplay hanging wall data coincide with the LWD data. Data from the other tectonic settings deviate partly to a greater extent.

5.2. *P* and *S* Wave Velocities With Increasing Confining Pressure

During the stage of pressure increase in the experiments, two characteristic features of V_p can be observed for all the samples. First, there is a constant to slightly increasing V_p with increasing effective confining pressure, and second, the velocities are significantly different for the four tectonic settings (see Figures 4a and 5a). Experimental pressurization was carried out under drained conditions, with pore water being squeezed out of the samples. Reduction of the pore water volume is indicative of the pore space reduction, which is the dominant control on velocity [*Wyllie et al*., 1956; *Erickson and Jarrard*, 1998; *Mavko et al*., 1998]. From synchrotron texture analysis of the experimental deformed sample material it is evident that the degree of crystallographic preferred orientation increases during the experimental deformation (K. Schumann et al., submitted manuscript, 2013). V_p in clay minerals is highest parallel to the basal plane and lowest parallel to the *c* axis [*Hamilton*, 1970; *Franklin and Mattson*, 1972]. Reorientation of the clay minerals with the basal planes perpendicular to the principal stress direction, and thus the direction of the lowest V_p parallel to the wave path, counteracts the velocity increase resulting from the increased pressure conditions [*Mondol et al*., 2007]. For this reason, V_p is rather constant or only slightly increases during the stage of pressure increase.

The varying V_p data for the different tectonic settings are probably due to structural (microfabric) and/or mineralogical differences and different initial porosities. Prism toe sediments are affected by overconsolidation because of erosion of the original overburden as well as tectonic deformation [e.g., *Kinoshita et al*., 2009; *Screaton et al*., 2009; *Tsuji et al*., 2011], while samples from the footwall and the hanging wall of the megasplay fault represent a normally sedimented slope cover without significant tectonic overprinting [*Expedition 316 Scientists*, 2009a; *Kinoshita et al*., 2009]. Lateral tectonic loading as well as overconsolidation at the accretionary prism toe decrease the porosity in comparison to samples of the megasplay fault area or the incoming plate from similar depth (Table 2) and enhance the grain-grain contacts of the sediments [*Stoll*, 1989; *Erickson and Jarrard*, 1998; *Gettemy and Tobin*, 2003; *Hashimoto et al*., 2011; *Raimbourg et al*., 2011]. Resulting V_p data of the prism toe are higher than those from the other three settings (Figures 5 and 6). Samples from the incoming plate are richer in clay minerals and are not affected by deformation and overconsolidation [cf. *Expedition 333 Scientists*, 2012a, 2012b; *Stipp et al*., 2013]. They show the highest porosities and the lowest velocities in our data (Figure 6).

The *S* wave velocity is defined as the ratio of the shear modulus and the density (see equation (2)). Since water does not transfer shear impulses, *S* waves cannot propagate through liquids. For this reason, decreasing pore water content due to increasing confining pressure increases V_s [*Toksöz et al*., 1976; *Mondol et al*., 2007]. As a consequence, lower pore water content leads to an increase of the interparticle coupling and friction which additionally enhances the *S* wave propagation [*Wyllie et al*., 1956; *Bourbié et al*., 1987; *Mondol et al*., 2007]. Both effects are reflected by the consistently increasing V_s values of the samples with increasing effective confining pressure (Figures 4b and 5b). Unlike the case of the *P* wave velocities (Figures 4a and 5a), the *S* wave velocities show no clear differentiation with respect to the accretionary prism toe and megasplay fault tectonic settings, but the two samples from the incoming plate have lower *S* wave velocities (see Figure 5b). This is probably caused by the higher porosities and the higher clay contents of the incoming plate sediments in comparison to all other samples.

The lithology control on *P* and *S* wave velocities is known to be weak [*Erickson and Jarrard*, 1998; *Raimbourg et al*., 2011], but the clay content directly changes the porosity, which exerts a primary control on the velocities [*Han and Nur*, 1986; *Marion et al*., 1992; *Hoffman and Tobin*, 2004; *Tsuji et al*., 2011]. Increasing clay content causes increasing porosities and thus decreasing *P* and *S* wave velocities [*Erickson and Jarrard*, 1998]. Additionally, this effect of increasing porosities is amplified by decreased interparticle coupling due to electrostatic repulsion of the clay minerals [*Chiou et al*., 1991; *Mitchell*, 1993].

5.3. *P* and *S* Wave Velocities During Triaxial Deformation

As triaxial deformation in the experiments was conducted under consolidated and undrained conditions, porosity and density of the samples should be constant at this stage. Water is incompressible at the given very low confining pressures. Hence, there should be little influence on *P* wave velocities by changes in pore water pressure. Indeed, V_p is rather constant during deformation with only a slight increase in a few of the data sets (Figures 6a and 6a). This small increase can reflect fabric changes with increasing strain and/or grain-to-grain contact with increasing effective axial stress. What remains different during deformation are the V_p values from the different tectonic settings. Samples from the toe of the accretionary wedge show higher V_p data than the samples from the megasplay fault area and the hemipelagic soft sediments from the incoming plate (Figures 6a and 7a). This difference is likely preserved from the pressurization stage (Figures 4a and 5a), during which the prism toe samples displayed the highest V_p data, while the measured velocities of the other tectonic settings largely overlap. Such a continuation in V_p data from drained pressure increase to undrained deformation stage can be seen when comparing velocities of the related diagrams, i.e., Figures 4a and 6a and Figures 5a and 7a, respectively.

In contrast to V_p, V_s values clearly increase with increasing effective axial stress during the deformation stage of the experiments (Figures 6b and 7b). Without measurable porosity and pore water effects during deformation (as explained above) and at the given constant composition, solely the microstructural rearrangement (shape-preferred orientation and crystallographic preferred orientation development) due to increasing strain and increasing grain to grain contacts with increasing principal stress can cause the strongly increasing V_s values in these experiments. Similar to V_p, V_s is the highest parallel to the basal plane. The increasing V_s could be due to an increasing crystallographic preferred orientation of the clay minerals (mainly illite and kaolinite) with increasing strain (cf. K. Schumann et al., submitted manuscript). Since V_s increases during the stage of experimental deformation while the clay minerals align perpendicular to the shortening axis, it becomes obvious that higher interparticle coupling due to clay mineral reorientation and increased principal effective stress causes the V_s increase and not the crystallographic preferred orientation itself. Samples from all tectonic settings largely overlap in their V_s $\sigma 1_{eff}$ trend. Only the hemipelagic soft sediments from the incoming plate show somewhat lower V_s data for a given effective axial stress (Figure 7b), which we attribute to the higher intial porosities and the higher clay content of these samples. This is in agreement to the slightly lower V_s values of the incoming plate samples during the stage of pressure increase just before starting the triaxial deformation (Figure 5b).

5.4. Shear Parameters

As unconsolidated sediments have high water contents, and interparticle coupling is weak, the initial V_p/V_s ratio is expected to be high. It will decrease during the course of compaction and deformation in the experiments [*Tsuji et al*., 2011; *Zimmer et al*., 2002], a fact that is evident from our data (Figures 10 and 11). The deformation stages were conducted under undrained conditions. For this reason, pore water content and pore space are constant. At increasing effective axial stresses, more grain-grain contacts result in higher V_s and lower V_p/V_s ratios. Anomalous trends, i.e., increasing V_p/V_s ratios and increasing Poisson's ratios with increasing effective axial stress, as observed for sample K003 (Figures 10b and 11b) reflect increasing pore pressure and related pore space collapse induced by deformation.

Previous studies [e.g., *Pickett*, 1963; *Tsuji et al*., 2011] have used the V_p/V_s ratio as an indicator for the state of consolidation. This is reflected in the pressure stepping test results (Figure 10a), where the normally consolidated samples from the incoming plate have somewhat higher V_p/V_s ratios than those from the other tectonic settings. On the other hand, this may simply be related to the higher clay content in the incoming plate sediments [cf. *Eastwood and Castagna*, 1986]. In the geoacoustic results of our study, overconsolidation due to material removal from IODP Sites C0006 and C0007 (accretionary prism toe) [*Screaton et al*., 2009] and from IODP Site C0008 (footwall of the megasplay fault) [*Kimura et al*., 2011; *Conin et al*., 2011; *Strasser et al*.,

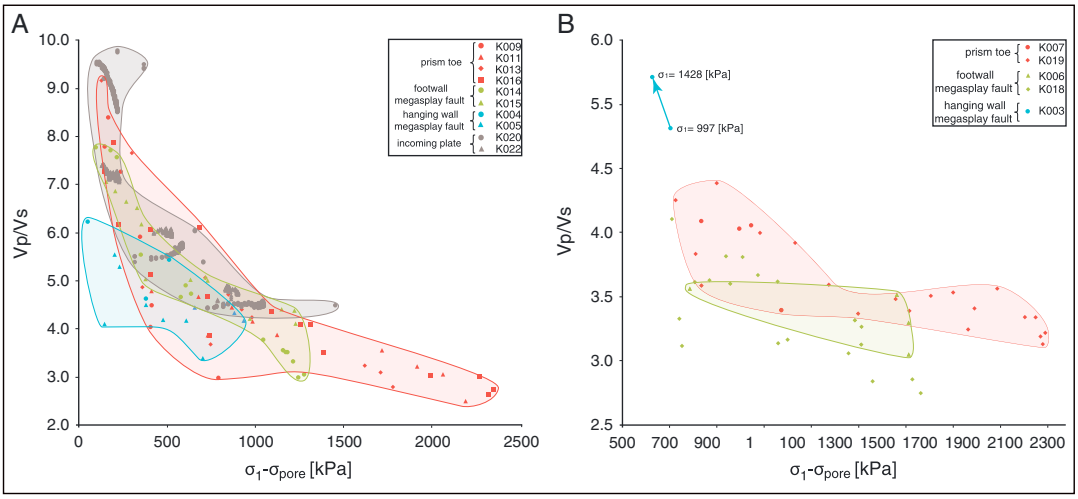

Figure 10. (a) Plot of V_p/V_s ratio versus the effective axial stress (σ_1-pore water pressure) measured during triaxial deformation of the pressure stepping tests. Between the deformation stages, confining pressure was increased in three steps (from 300 to 400 kPa, from 400 to 640 kPa, and from 640 to 1000 kPa). (b) Plot of V_p/V_s ratio versus the effective axial stress (σ_1-pore water pressure) of the single-step compression and the rate stepping tests. Blue arrow indicates decrease in effective largest principal stress in experiment K003 due to a strongly increasing pore water pressure. Values for the increasing principal stress are indicated.

2011] is not obvious, when the V_p/V_s ratios (Figure 10) and Poisson's ratios (Figure 11) are compared between overconsolidated (prism toe, megasplay footwall) and normally consolidated (incoming plate, megasplay hanging wall) settings.

The shear moduli determined in this study range between 0.2 and 1.37 GPa, and the bulk moduli range between 3.85 and 8.41 GPa (Table 4). *Hashimoto et al*. [2011] presented shear and bulk moduli data from Site C0002 of IODP Expedition 315 and Site C0004 of IODP Expedition 316. In this study, only one sample from similar depth is described (97 mbsf). The shear modulus of this sample is 0.79 GPa, and the bulk modulus is 4.18 GPa [*Hashimoto et al*., 2011], thus being in the range of the values in our study.

The low shear, bulk, and elastic moduli determined for samples from the incoming plate and the hanging wall of the megasplay fault are indicative of a lower degree of consolidation. The highest values were measured for the accretionary prism toe sediments, indicating overconsolidation due to erosional material removal [*Screaton et al*., 2009] and tectonic overprint at the accretionary prism toe. At the footwall of the megasplay

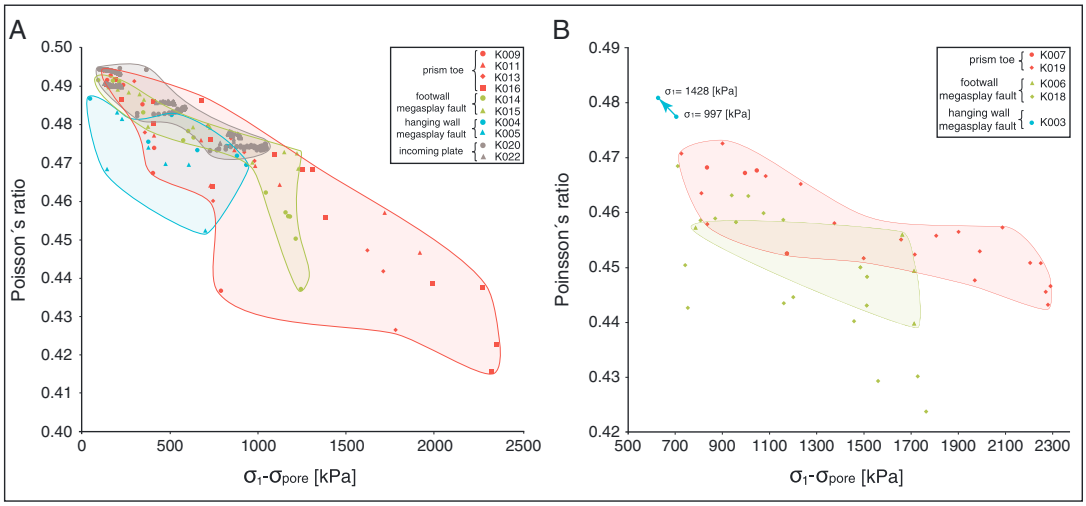

Figure 11. (a) Plot of Poisson's ratio versus the effective largest principal stress (σ_1-pore water pressure) measured during triaxial deformation of the pressure stepping tests. Confining pressure steps are from 300 to 400 kPa, from 400 to 640 kPa, and from 640 to 1000 kPa. (b) Plot of Poisson's ratio versus the effective largest principal stress (σ_1-pore water pressure) measured during triaxial deformation of the single-step compression and the rate stepping tests. Blue arrow indicates decrease in effective largest principal stress in experiment K003 due to a strongly increasing pore water pressure. Values for the increasing largest principal stress are indicated.

fault, the shear, bulk, and elastic moduli are higher than those from the incoming plate and the megasplay hanging wall. Again, this is attributed to erosional material removed at Site C0008 [*Kimura*, 2011; *Conin et al*., 2011; *Strasser et al*., 2011], resulting in slight overconsolidation in these near-surface sediments.

6. Summary and Conclusions

Although frequencies used were not optimal for the sample lengths (especially for *P* waves), the new method of data processing yields reliable information on *P* and *S* wave velocities. This is shown by reference measurements with high data redundancy (samples K020 and K022). Optical single trace first arrival detection performed in the laboratory during the triaxial deformation tests resulted in picking strong reflections not belonging to first arrivals. Instead, multiple and reflected signals were picked. In case of the *S* waves, however, first raw picking yielded good results. Time series analysis and manually picked first arrivals in common shear test gathers helped to identify erroneous signals. In combination with filters and static corrections, first arrival detection was refined and data quality could be checked by visualization as color-coded wiggle plots.

The measured *P* wave velocities differ slightly depending on the tectonic setting, with highest velocities measured for the accretionary prism toe sediments ranging from ~1650 to ~2200 m/s and lowest velocities measured for the incoming plate sediments ranging from ~1450 to ~1650 m/s. In contrast, *S* wave velocities are similar in all tectonic settings ranging from ~150 to ~780 m/s. As a result, parameters like V_p/V_s ratios, shear, bulk, and the elastic moduli can be used to characterize tectonic settings in an environment of only subtle compositional differences of the sediments. Most probably, these differences result from different compaction paths and deformation histories. Sediments from the accretionary prism toe are influenced by tectonic compaction, which decreases porosity and increases stiffness, resulting in higher velocities. The elastic moduli point to less consolidated sediments on the incoming plate and the hanging wall of the megasplay fault, unaffected by deformation and tectonic overprinting. Overconsolidation due to erosional material removal and tectonic overprint is reflected in highest elastic moduli found in sediments from the accretionary prism toe. Elastic moduli from the footwall of the megasplay fault are intermediate, reflecting a lesser degree of overconsolidation.

In general, the analysis confirms previous observations regarding the dependence of V_p and V_s on parameters such as porosity, pore water content, effective confining pressure, and effective axial stress of deep marine sediments. The data show that V_p is correlated to porosity and mineralogy of the samples and, to a minor extent, to the confining pressure and stress conditions prevailing during the experiments. In the case of V_s, the increasing grain-grain contacts positively influence wave propagation, as shown by the velocity increases with increasing effective stress.

Acknowledgments

This study used samples and data provided by the Integrated Ocean Drilling Program (IODP). The authors would like to thank the Scientific Parties of IODP Expeditions 315, 316, and 333 aboard D/V *CHIKYU* for sample collection and data acquisition. Furthermore, we would like to thank Y. Kitamura, V. Feeser, M. Rolfs, and R. Hinkes for samples supply, technical support, and discussions of the triaxial test data. This work was funded by the Deutsche Forschungsgemeinschaft (DFG) through grant BE1041/28 to J.H.B. and M.S. We also thank Editor A. Revil, Associated Editor D. Faulkner, and reviewers Y. Hashimoto and B. Carpenter for very thorough and helpful reviews.

References

Ando, M. (1975), Source mechanisms and tectonic significance of historical earthquakes along the Nankai Trough, Japan, *Tectonophysics*, *27*, 119–140.

Arulnathan, R., R. W. Boulanger, and M. F. Riemer (1998), Analysis of bender element tests, *Geotech. Test. J.*, *21*(2), 120–131.

Baba, T., and P. R. Cummins (2005), Contiguous rupture areas of two Nankai Trough earthquakes revealed by high-resolution tsunami waveform inversion, *Geophys. Res. Lett.*, *32*, L08305, doi:10.1029/2004GL022320.

Baba, T., P. R. Cummins, T. Hori, and Y. Kaneda (2006), High precision slip distribution of the 1944 Tonankai earthquake inferred from tsunami waveforms: Possible slip on a splay fault, *Tectonophysics*, *426*, 119–134.

Becker, J. J., et al. (2009), Global bathymetry and elevation data at 30 arc seconds resolution: SRTM30_PLUS, *Mar. Geod.*, *32*(4), 355–371.

Bilek, S. L., and T. Lay (1999), Rigidity variations with depth along interplate megathrust faults in subduction zones, *Lett. Nat.*, *400*, 443–446.

Bourbié, T., O. Coussy, and B. Zinszner (1987), *Acoustics of Porous Media*, Editions Technip, Paris.

Carson, B., R. von Huene, and M. Arthur (1982), Small-scale deformation structures and physical properties related to convergence in Japan Trench slope sediments, *Tectonics*, *1*(3), 277–302.

Chiou, W. A., W. R. Bryant, and R. H. Bennet (1991), Clay fabric of gassy submarine sediments, in *Microstructure of Fine-Grained Sediments*, edited by R. H. Bennet, W. R. Bryant, and M. H. Hulbert, pp. 5–32, Springer-Verlag, New York.

Conin, M., P. Henry, S. Bourlange, H. Raimbourg, and T. Reuschlé (2011), Interpretation of porosity and LWD resistivity from the Nankai accretionary wedge in light of clay physicochemical properties: Evidence for erosion and local overpressuring, *Geochem. Geophys. Geosyst.*, *12*, Q0AD07, doi:10.1029/2010GC003381.

DIN 18137 (2011) Soil, investigation and testing—Determination of shear strength—Part2: Triaxial test (German industry standards), Deutsches Institut für Normung, Berlin, Germany.

Dyvik, R., and C. Madshus (1985), Lab measurements of G_{max} using bender elements, in *Advances in the Art of Testing Soils Under Cyclic Conditions*, edited by V. Khosla, pp. 186–196, American Society of Civil Engineers, New York.

Eastwood, R. L., and J. P. Castagna (1986), Interpretation of V_p/V_s ratio from sonic logs, in *Shear-wave exploration*, edited by S. N. Domenico, pp. 139–153, Society of exploration geophysics, Tulsa, Okla.

Erickson, S., and R. Jarrard (1998), Velocity-porosity relationship for water-saturated siliciclastic sediments, *J. Geophys. Res.*, *103*(B12), 30,385–30,406.
Expedition 315 Scientists (2009), Expedition 315 Site C0001, in *Proceedings of the International Ocean Drilling Program*, vol. 314/315/316, edited by M. Kinoshita et al., Integrated Ocean Drilling Program Management International, Inc., Washington, D. C., doi:10.2204/iodp.proc.314315316.123.2009.
Expedition 316 Scientists (2009a), Expedition 316 Site C0004, in *Proceedings of the International Ocean Drilling Program*, vol. 314/315/316, edited by M. Kinoshita et al., Integrated Ocean Drilling Program Management International, Inc., Washington, D. C., doi:10.2204/iodp.proc.314315316.133.2009.
Expedition 316 Scientists (2009b), Expedition 316 Site C0006, in *Proceedings of the International Ocean Drilling Program*, vol. 314/315/316, edited by M. Kinoshita et al., Integrated Ocean Drilling Program Management International, Inc., Washington, D. C., doi:10.2204/iodp.proc.314315316.134.2009.
Expedition 316 Scientists (2009c), Expedition 316 Site C0007, in *Proceedings of the International Ocean Drilling Program*, vol. 314/315/316, edited by M. Kinoshita et al., Integrated Ocean Drilling Program Management International, Inc., Washington, D. C., doi:10.2204/iodp.proc.314315316.135.2009.
Expedition 316 Scientists (2009d), Expedition 316 Site C0008, in *Proceedings of the International Ocean Drilling Program*, vol. 314/315/316, edited by M. Kinoshita et al., Integrated Ocean Drilling Program Management International, Inc., Washington D. C., doi:10.2204/iodp.proc.314315316.136.2009.
Expedition 316 Scientists (2009e), Expedition 316 methods, in *Proceedings of the International Ocean Drilling Program*, vol. 314/315/316, edited by M. Kinoshita et al., Integrated Ocean Drilling Program Management International, Inc., Washington, D. C., doi: 10.2204/iodp.proc.314315316.132.2009.
Expedition 333 Scientists (2012a), Expedition 333 Site C0011, in *Proceedings of the International Ocean Drilling Program*, vol. 333, edited by P. Henry et al., Integrated Ocean Drilling Program Management International, Inc., Tokyo, doi:10.2204/iodp.proc.333.104.2012.
Expedition 333 Scientists (2012b), Expedition 333 Site C0012, in *Proceedings of the International Ocean Drilling Program*, vol. 333, edited by P. Henry et al., Integrated Ocean Drilling Program Management International, Inc., Tokyo, doi:10.2204/iodp.proc.333.105.2012.
Franklin, A. G., and P. A. Mattson (1972), Directional variation of elastic wave velocities in oriented clay, *Clays Clay Miner.*, *20*, 285–293.
Gettemy, G. L., and H. J. Tobin (2003), Tectonic signatures in centimeter-scale velocity-porosity relationships of Costa Rica convergent margin sediments, *J. Geophys. Res.*, *180*(B10), 2494, doi: 10.1029/2001JB000738.
Hamilton, E. L. (1970), Sound velocity and related properties of marine sediments, North Pacific, *J. Geophys. Res.*, *75*(23), 4423–4446.
Hamilton, E. L., and R. T. Bachman (1982), Sound velocity and related properties of marine sediments, *J. Acoust. Soc. Am.*, *72*(6), 1891–1904.
Han, D., and A. Nur (1986), Effects of porosity and clay content on wave velocities in sandstones, *Geophysics*, *51*, 2093–2107, doi:10.1190/1.1442062.
Hashimoto, Y., H. Tobin, and M. Knuth (2010), Velocity-porosity relationship for slope apron and accreted sediments in the Nankai Trough Seismogenic Zone Experiment, Integrated Ocean Drilling Program Expedition 315 Site C0001, *Geochem. Geophys. Geosyst.*, *11*, Q0AD05, doi:10.1029/2010GC003217.
Hashimoto, Y., H. J. Tobin, M. Knuth, and A. Harada (2011), Data report: Compressional and shear wave velocity measurements on sediment in the hanging wall and the footwall of megasplay fault, NanTroSEIZE Stage 1, in *Proceedings of the Integrated Ocean Drilling Program*, vol. 314/315/316, edited by M. Kinoshita et al., Integrated Ocean Drilling Program Management International, Inc., Washington, D. C., doi:10.2204/iodp.proc.314315316.217.2011.
Hoffman, N. W., and H. J. Tobin (2004), An empirical relationship between velocity and porosity for underthrust sediments in the Nankai Trough accretionary prism, *Proc. Integrated Ocean Drill. Program Sci. Results*, *190–196*, 1–23.
Hyndman, R. D., G. F. Moore, and K. Moran (1993), Velocity, porosity, and pore-fluid loss from the Nankai subduction zone accretionary prism, *Proc. Integrated Ocean Drill. Program Sci. Results*, *131*, 211–220.
Johnston, J. E., and N. I. Christensen (1993), Compressional to shear velocity ratios in sedimentary rocks, *Int. J. Rock Mech. Min. Sci. Geomech. Abstr.*, *30*(7), 751–754.
Kimura, G., G. F. Moore, E. Screaton, D. Curewitz, C. Streiff, and H. Tobin (2011), Spatial and temporal evolution of the megasplay fault in the Nankai Trough, *Geochem. Geophys. Geosyst.*, *12*, Q0A008, doi:10.1029/2010GC003335.
Kinoshita, M., H. Tobin, J. Ashi, G. Kimura, S. Lallemant, E. J. Screaton, D. Curewitz, H. Masago, K. T. Moe, and the Expedition 314/315/316 Scientists (2009), *Proc. IODP*, vol. 314/315/316, Integrated Ocean Drilling Program Management International, Inc., Washington, D. C., doi:10.2204/iodp.proc.314315316.123.2009.
Kinoshita, M., H. Tobin, N. Eguchi, and N. Simon (2012), IODP Expedition 326 Operations: First stage of Nankai Trough plate boundary riser drilling, *Sci. Drill.*, *4*, 30–33, doi:10.2204/iodp.sd.14.03.2012.
Kitajima, H., F. M. Chester, and G. Biscontin (2012), Mechanical and hydraulic properties of Nankai accretionary prism sediments: Effect of stress path, *Geochem. Geophys. Geosyst.*, *13*, Q0AD27, doi:10.1029/2012GC004124.
Lee, J., and C. Santamarina (2005), Bender elements: Performance and signal interpretation, *J. Geotech. Geoenviron. Eng.*, *131*(9), 1063–1070, doi:10.1061/(ASCE)1090-0241(2005)131:9(1063.
Leong, E. C., S. H. Yeo, and H. Rahardjo (2005), Measuring shear wave velocity using bender elements, *Geotech. Test. J.*, *28*(5), 488–498.
Marion, D., A. Nur, H. Yin, and D. Han (1992), Compressional velocity and porosity in sand-clay mixtures, *Geophysics*, *57*(4), 554–563.
Mavko, G., T. Mukerji, and J. Dvorkin (1998), *The Rock Physical Handbook, Tool for Seismic Analysis in Porous Media*, 329 pp., Cambridge Univ. Press, Cambridge, U. K.
Milliken, K. L., and R. M. Reed (2010), Multiple causes of diagenetic fabric anisotropy in weakly consolidated mud, Nankai accretionary prism, IODP Expedition 316, *J. Struct. Geol.*, *32*, 1887–1898.
Mitchell, J. K. (1993), *Fundamentals of Soil Behavior*, 2nd ed., Wiley, New York.
Mondol, N. H., K. Bjørlykke, J. Jahren, and K. Høeg (2007), Experimental mechanical compaction of clay mineral aggregates—Changes in physical properties of mudstones during burial, *Mar. Pet. Geol.*, *24*, 289–311.
Moore, G. F., N. L. Bangs, A. Taira, S. Kuramoto, E. Pangborn, and H. J. Tobin (2007), Three-dimensional splay fault geometry and implications for tsunami generation, *Science*, *318*, 1128–1131, doi:10.1126/science.1147195.
Moore, G. F., J. Park, N. L. Bangs, S. P. Gulick, H. J. Tobin, Y. Nakamura, S. Sato, T. Tsuji, T. Yoro, H. Tanaka, S. Uraki, Y. Kido, Y. Sanada, S. Kuramoto, and A. Taira (2009), Structural and seismic stratigraphic framework of the NanTroSEIZE Stage 1 transect, in *Proceedings of the IODP*, *314/315/316*, edited by M. Kinoshita et al., Integrated Ocean Drilling Program Management International, Inc., Washington, D. C., doi:10.2204/iodp.proc.314315316.102.2009.
Moore, J. C., and D. Saffer (2010), Updip limit of the seismogenic zone beneath the accretionary prism of southwest Japan: An effect of diagenetic to low-grade metamorphic processes and increasing effective stress, *Geology*, *29*(2), 183–186, doi:10.1130/0091-7613(2001)029<0183:ULOTSZ>2.0.CO;2.

Moore, J. C., and P. Vrolijk (1992), Fluids in accretionary prisms, *Rev. Geophys.*, *30*(2), 113–135.
Nakamura, K., K. Shimazaki, and N. Yonekura (1984), Subduction bending and education. Present and Quaternary tectonics of the northern border of the Philippine Sea Plate, *Bull. Soc. Geol. Fr.*, *26*(2), 221–243.
Park, J., T. Tsuru, S. Kodaira, A. Nakanishi, S. Miura, Y. Kaneda, and Y. Kono (2000), Out-of-sequence thrust faults developed in the coseismic slip zone of the 1946 Nankai earthquake (*Mw* = 8.2) off Shikoku, southwest Japan, *Geophys. Res. Lett.*, *27*(7), 1033–1036.
Park, J., T. Tsuru, S. Kodaira, R. Cummins, Y. Kaneda (2002a), Splay fault branching along the Nankai subduction zone, *Science*, *297*, 1157–1160, doi:10.1126/science.1074111.
Park, J., T. Tsuru, N. Takahashi, T. Hori, S. Kodaira, A. Nakanishi, S. Miura, and Y. Kaneda (2002b), A deep strong reflector in the Nankai accretionary wedge from multichannel seismic data: Implications for underplating and interseismic stress release, *J. Geophys. Res.*, *107*(B4), 2061, doi:10.1029/2001JB000262.
Pickett, G. R. (1963), Acoustic character logs and their application in formation evaluation, *J. Can. Pet. Technol.*, *15*, 659–667.
Quantachrome Corporation (2011–2013), Pentapycnometer manual, http://www.quantachrome.com/instruments.html.
Raimbourg, H., Y. Hamano, S. Saito, M. Kinoshita, and A. Kopf (2011), Acoustic and mechanical properties of Nankai accretionary prism core samples, *Geochem. Geophys. Geosyst.*, *12*, Q0AD10, doi:10.1029/2010GC003169.
Saffer, D., J. Guo, M. B. Underwood, W. Likos, R. M. Skarbek, I. Song, and M. Gildow (2011), Date report: Consolidation, permeability, and fabric of sediments from the Nankai continental slope, IODP Sites C0001, C0008, and C0004, in *Proceedings of the Integrated Ocean Drilling Program*, edited by M. Kinoshita et al., Washington, D. C.
Santamarina, J. C., and M. A. Fam (1997), Interpretation of bender element tests—Discussion, *Geotechnique*, *47*(4), 873–877.
Scholz, C. H. (2002), *The Mechanics of Earthquakes and Faulting*, 2nd ed., Cambridge Univ. Press, Cambridge, U. K.
Screaton, E., et al. (2009), Interactions between deformation and fluids in the frontal thrust region of the NanTroSEIZE transect offshore the Kii Peninsula, Japan: Results from IODP Expedition 316 Sites C0006 and C0007, *Geochem. Geophys. Geosyst.*, *10*, Q0AD01, doi:10.1029/2009GC002713.
Seno, T., S. Stein, and A. E. Gripp (1993), A model for the motion of the Philippine Sea plate consistent with NUVEL-1 and geological data, *J. Geophys. Res.*, *98*(B10), 17,941–17,948.
Shumway, G. (1960), Sound speed and absorption studies of marine sediments by a resonance method. Part I, *Geophysics*, *25*(2), 451–467.
Stipp, M., M. Rolfs, Y. Kitamura, J. H. Behrmann, K. Schumann, D. Schulte-Kortnack, and V. Feeser (2013), Strong sediments at the deformation front, and weak sediments at the rear of the Nankai accretionary prism, revealed by triaxial deformation experiments, *Geochem. Geophys. Geosyst.*, *14*, 4791–4810, doi:10.1002/ggge.20290.
Stoll, R. D. (1989), *Sediment Acoustics*: New York Springer Verlag, Lecture Notes in Earth Sciences, *26*.
Strasser, M., G. F. Moore, G. Kimura, A. Kopf, M. B. Underwood, J. Guo, and E. Screaton (2011), Slumping and mass transport deposition in the Nankai fore arc: Evidence from IODP drilling and 3-D reflection seismic data, *Geochem. Geophys. Geosyst.*, *12*, Q0AD13, doi:10.1029/2010GC003431.
Taira, A. (2001), Tectonic evolution of the Japanese island arc system, *Annu. Rev. Earth Planet. Sci.*, *29*, 109–134.
Taira, A., I. Hill, J. Firth, and Shipboard Scientific Party (1991), Geological background and objectives, *Proc. Ocean Drill. Program Initial Rep.*, *131*.
Timur, A. (1977), Temperature dependence of compressional and shear wave velocities in rocks, *Geophysics*, *42*(5), 950–956.
Tobin, H., and M. Kinoshita (2006), NanTroSEIZE: The IODP Nankai Trough seismogenic zone experiment, *Sci. Drill.*, *2*, 23–27, doi:10.2204/iodp.sd.2.06.2006.
Toksöz, M. N., C. H. Cheng, and A. Timur (1976), Velocities of seismic waves in porous rocks, *Geophysics*, *41*(4), 621–645.
Tsuji, T., J. Dvorkin, G. Mavko, N. Nakata, T. Matsuoka, A. Nakanishi, S. Kodaira, and O. Nishizawa (2011), V_p/V_s ratio and shear-wave splitting in the Nankai Trough seismogenic zone: Insights into effective stress, pore pressure, and sediment consolidation, *Geophysics*, *76*(3), 71–82, doi:10.1190/1.3560018.
Viggiani, G., and J. H. Atkinson (1995), Interpretation of bender element tests, technical note, *Geotechnique*, *45*(1), 149–154.
Wang, K., and Y. Hu (2006), Accretionary prisms in subduction earthquake cycles: The theory of dynamic Coulomb wedge, *J. Geophys. Res.*, *111*, B06410, doi:10.1029/2005JB004094.
Wyllie, M. R. J., A. R. Gregory, and L. W. Gardner (1956), Elastic wave velocity in heterogeneous and porous media, *Geophysics*, *21*(1), 41–70.
Xu, J., and Y. Kono (2002), Geometry of slab, intraslab stress field and its tectonic implication in the Nankai trough, Japan, *Earth Planets Space*, *54*, 733–742.
Zimmer, M., M. Prasad, and G. Mavko (2002), Pressure and porosity influences on V_p-V_s ratio in unconsolidated sands, *Leading Edge*, *21*, 178–183, doi:10.1190/1.1452611.